UDK 669.14.018.8:537.226.86
Original scientific article/Izvirni znanstveni članek

ISSN 1580-2949
Mater. Tehnol.

STUDY ON THERMAL DEFORMATION OF AS-CAST S32101 ECONOMICAL DUPLEX STAINLESS STEEL

ŠTUDIJ TOPLOTNE DEFORMACIJE STANDARDNE DUPLEKS NERJAVNE JEKLENE LITINE TIPA S32101

Ming Zhao[1], Huaying Li[13]*, Xiaogang Wang[4], Guanzheng Su[1], Fang Huang[1], Qi Chen[1], Yibo Lu[2]

[1]School of Materials Science and Engineering, Taiyuan University of Science and Technology, Taiyuan 030024, Shanxi, China
[2]School of Mechanical Engineering, Taiyuan University of Science and Technology, Taiyuan 030024, Shanxi, China
[3]National Key Laboratory of Advanced Stainless Steel, Taiyuan, 030024, Shanxi, China
[4]Engineering Research Center Heavy Machinery Ministry of Education, Taiyuan University of Science and Technology, Taiyuan 030024, Shanxi, China

Prejem rokopisa – received: 2025-02-18; sprejem za objavo – accepted for publication: 2025-05-15

doi:10.17222/mit.2025.1397

This study investigates the hot deformation behavior of cast S32101 duplex stainless steel through hot compression tests conducted at temperatures ranging from 950 °C to 1200 °C and strain rates of 0.01–10 s–1, with a true strain of 0.916. Electron backscatter diffraction (EBSD) was used for characterization to explore the thermodynamic behavior, hot deformation map, and microstructural evolution during the deformation process. True stress-strain curves were generated under various deformation conditions, and a high-precision Arrhenius-based constitutive model was developed. Microstructural analysis revealed that at 1100 °C/10 s^{-1} and 1150 °C/0.01 s^{-1}, both ferrite and austenite phases deformed uniformly. At 1150 °C, dynamic recrystallization (DRX) was promoted in the austenite phase as the strain rate increased from 0.01 s^{-1} to 10 s^{-1}. At 950 °C/0.1–10 s^{-1}, severe deformation occurred in the microstructure. The primary recovery mechanisms for the austenite phase at low and high temperatures were dynamic recovery (DRV) and dynamic recrystallization (DRX), respectively. The ferrite phase softened through continuous dynamic recrystallization. A dynamic material model (DMM) hot-deformation map was established, revealing the optimal processing windows to be 950–1200 °C/0.01 s^{-1} and 1100 °C/0.01–10 s^{-1}.

Keywords: economical duplex stainless steel, thermal deformation behavior, microstructure evolution, recrystallization, hot working map

V članku avtorji opisujejo študijo obnašanja konvencionalne nerjavne jeklene litine vrste S32101 med vročo deformacijo. Preizkuse vročega stiskanja jeklene litine so izvajali pri temperaturah med 950 °C in 1200 °C, hitrostih deformacije med 0,01 s^{-1} in 10 s^{-1} ter pravi deformaciji 0,916. Avtorji so zato, da bi preučili termodinamično obnašanje litine, razvili zemljevid vroče predelave, preučili razvoj mikrostrukture med postopkom deformacije in izvedli karakterizacijo deformirane litine s pomočjo difrakcije (uklona) povratno sipanih elektronov (EBSD; angl.: electron back scattered diffraction). Izdelali so krivulje *prava napetost – prava deformacija* za različne pogoje deformacije in razvili zelo natančen Arrheniusov konstitutivni (temeljni) model. Mikrostrukturna analiza je pokazala, da sta pri 1100 °C/10 s^{-1} in 1150 °C/0,01 s^{-1} obe fazi, ferit in avstenit, enakomerno deformirani. Pri 1150 °C je bila dinamična rekristalizacija (DRX) v avstenitni fazi spodbujena, ko je hitrost deformacije narasla z 0,01 s^{-1} na 10 s^{-1}. Pri 950 °C in vseh izvedenih hitrostih deformacije je prišlo do močne deformacije mikrostrukture. Glavna mehanizma spremembe austenitne faze, tako pri nizkih in visokih temperaturah, sta bila dinamična poprava (DRV) in dinamična rekristalizacija (DRX), medtem ko se je feritna faza mehčala zaradi kontinuirne dinamične rekristalizacije. Avtorji so razvili dinamični materialni model (DMM) za izdelavo zemljevida vroče predelave, ki kaže kje so optimalna področja vroče predelave v območjih med 950 °C in 1200 °C/0,01 s^{-1} ter 1100 °C/0,01–10 s^{-1}.

Ključne besede: standardna nerjavna jeklena litina, obnašanje nerjavne jeklene litine med termično deformacijo, razvoj mikrostrukture, rekristalizacija, grafikon ("zemljevid") vroče predelave

1 INTRODUCTION

Duplex stainless steel refers to stainless steel that contains both ferrite and austenite phases in its solid solution, with at least 30 % of one phase present by volume.[1,2] Duplex stainless steel combines the advantages of both ferritic and austenitic stainless steels. When appropriately controlling the chemical composition and heat treatment processes, duplex stainless steel exhibits the excellent toughness and good weldability of austenitic stainless steel, while also retaining the higher strength, resistance to pitting corrosion, crevice corrosion, wear corrosion, and chloride stress corrosion cracking of ferritic stainless steel.[3] However, the S32101 duplex stainless steel wire is prone to cracking during the rolling process, which significantly reduces its yield and production efficiency. According to the literature,[4] when both ferrite and austenite phases are present in stainless steel, cracks are likely to form at phase boundaries if improper process parameters are applied. Currently, research on S32101 economical duplex stainless steel has primarily focused on welding and corrosion aspects,[5,6] with limited attention given to its hot working processes. Therefore, in order to enhance the performance of S32101 economi-

---

*Corresponding author's e-mail:
2014246@tyust.edu.cn (Huaying Li)

cal duplex stainless steel and prevent cracking during processing, it is crucial to investigate the hot working processes of S32101 duplex stainless steel.

According to recent studies, constructing processing maps is one of the most widely used and effective methods for describing the hot-deformation behavior of metallic materials.[7] During the deformation process, various factors such as deformation temperature, strain, and strain rate influence the material behavior.[8] Constitutive models constructed from experimental data can effectively reflect the sensitivity of flow stress to temperature, strain, and strain rate. Currently, the Johnson-Cook (JC) model, Zerilli-Armstrong (ZA) model, and Arrhenius model are commonly used to describe the characteristics of hot deformation.[9] Samantaray et al.[10] developed three constitutive models for modified 9Cr-1Mo steel: the JC model, the improved Zerilli-Armstrong (MZA) model, and the SCA model. The results showed that the experimental data were in good agreement with the Arrhenius model, although the Arrhenius-type model requires a higher computational workload and more time to calculate the parameters. Processing maps based on the dynamic materials model (DMM) are often used to predict the deformation mechanisms and microstructural properties of materials under different deformation conditions, providing valuable analytical methods and material processing guidelines.[11]

During the hot-deformation process, materials undergo microstructural changes such as work hardening, dynamic recovery (DRV), and dynamic recrystallization (DRX). The occurrence of DRX plays a significant role in refining the grain size of stainless steel and improving the uniformity of the microstructure. Song et al.[12] used EBSD to study the microstructural evolution of 2205 duplex stainless steel during hot deformation and found that as the deformation rate increased, the content of austenite gradually increased, while the content of ferrite decreased. Regarding the hot-deformation behavior of MP159 high-temperature alloy, Cai et al.[13] observed that discontinuous DRX was the main cause for the nucleation of this alloy.

Based on the above findings, this study conducted isothermal compression tests at constant strain rates on cast S32101 economical duplex stainless steel to investigate its hot-deformation behavior within a processing temperature range of 950–1200 °C and strain rates of 0.01–10s^{-1}. An Arrhenius-type constitutive model was developed. A microstructural analysis of the quenched samples was performed using electron backscatter diffraction (EBSD). A processing map was constructed based on the flow curves to accurately describe the rheological behavior and hot processing characteristics.

2 EXPERIMENTAL AND MATERIALS

The experimental material used in this study included cast S32101 economical duplex stainless steel plates provided by Shanxi Tai Gang Group Co., Ltd. The chemical composition of the S32101 duplex stainless steel is shown in **Table 1**. The initial microstructure is shown in **Figure 1b**, where it can be observed that the cast microstructure has coarse grains, with ferrite distributed within the austenite matrix. Samples were taken from similar locations of the original cast specimens, and after grinding the end faces and outer surfaces with a grinder, the samples had dimensions of (10 × 15) mm and cylindrical shapes. The processed cylinders were subjected to uniaxial isothermal hot compression testing using a Gleeble-3800 thermal simulator. The testing process is shown in **Figure 1a**. Initially, the samples were heated to 1250 °C at a rate of 5 °C/s, followed by a 300-s holding time to ensure a more uniform microstructure. The samples were then cooled to different deformation temperatures (950, 1000, 1050, 1100, 1150, 1200) °C at a cooling rate of 5 °C/s, followed by a 30-s holding time. Compression tests were carried out at strain rates of (0.01, 0.1, 1, and 10) s^{-1}, with a deformation strain of 60 %. Tantalum foils and graphite lubricants were used

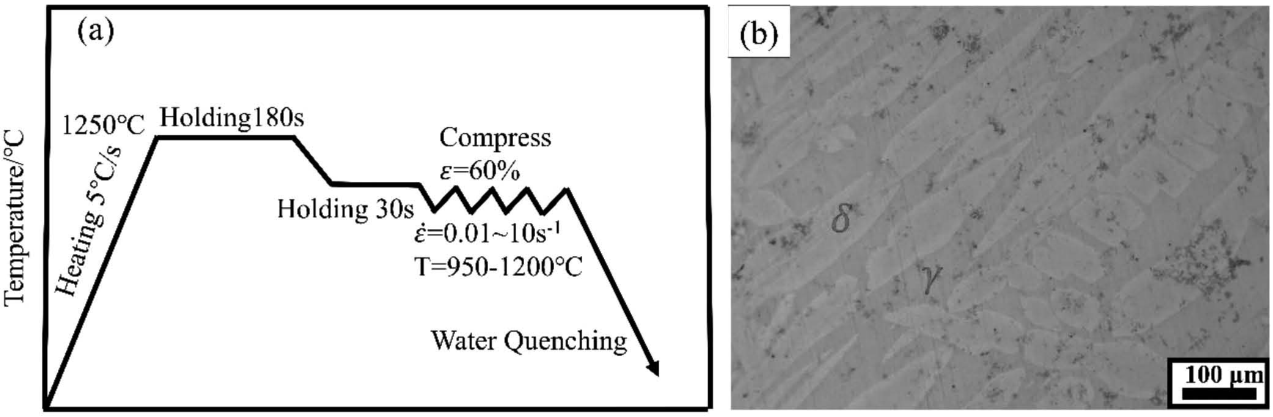

Figure 1: a) Experimental process of thermal compression, b) phase diagram of initial organization

between the compression heads and the sample to minimize friction effects during the experiment.

After compression, the samples were immediately quenched in water to preserve their high-temperature microstructure for subsequent microstructural analysis. The samples were then sectioned symmetrically along the longitudinal plane using wire electrical discharge machining (EDM), followed by grinding, polishing, and electrochemical polishing. The central region of the section was characterized using a step size of 0.9 μm with a ZEISS SIGMA 300 (equipped with EBSD). In this study, EBSD was used to distinguish the ferrite and austenite phases. In the subsequent analysis, ferrite and austenite are represented as BCC and FCC, respectively.

Table 1: Chemical composition of S32101 economical duplex stainless steel (%)

C	Si	Mn	P	S	Cr	Ni	Mo	Cu	N
0.02	0.51	5.14	0.017	0.001	21.51	1.58	0.15	0.15	0.21

3 RESULTS

3.1 Flow curve characteristics

The true stress-strain curves of S32101 economical duplex stainless steel are shown in **Figure 2**. As can be seen, when the strain rate ranges from 0.01 s^{-1} to 1 s^{-1}, the flow stress rapidly increases with the strain at the early stage of deformation. This is due to the generation of dislocations and strain hardening. Afterward, the flow stress slowly increases until it reaches a peak, after which it stabilizes. This steady state is attributed to dynamic softening mechanisms, including dynamic recovery (DRV) and dynamic recrystallization (DRX), which counteract the effects of strain hardening. Additionally, at 950 °C, clear yield platforms appear in the curves at strain rates of 0.01 s^{-1} and 0.1 s^{-1}. This yield platform behavior is typical of low-carbon steels and low-strength low-alloy steels, primarily caused by the "dragging" of dislocations by carbon-nitrogen atom clusters (Cottrell atmospheres). When the strain rate is 10 s^{-1}, a "yield-like platform" softening phenomenon forms at a true strain of approximately 0.13, which is consistent with the findings reported in the literature.[14]

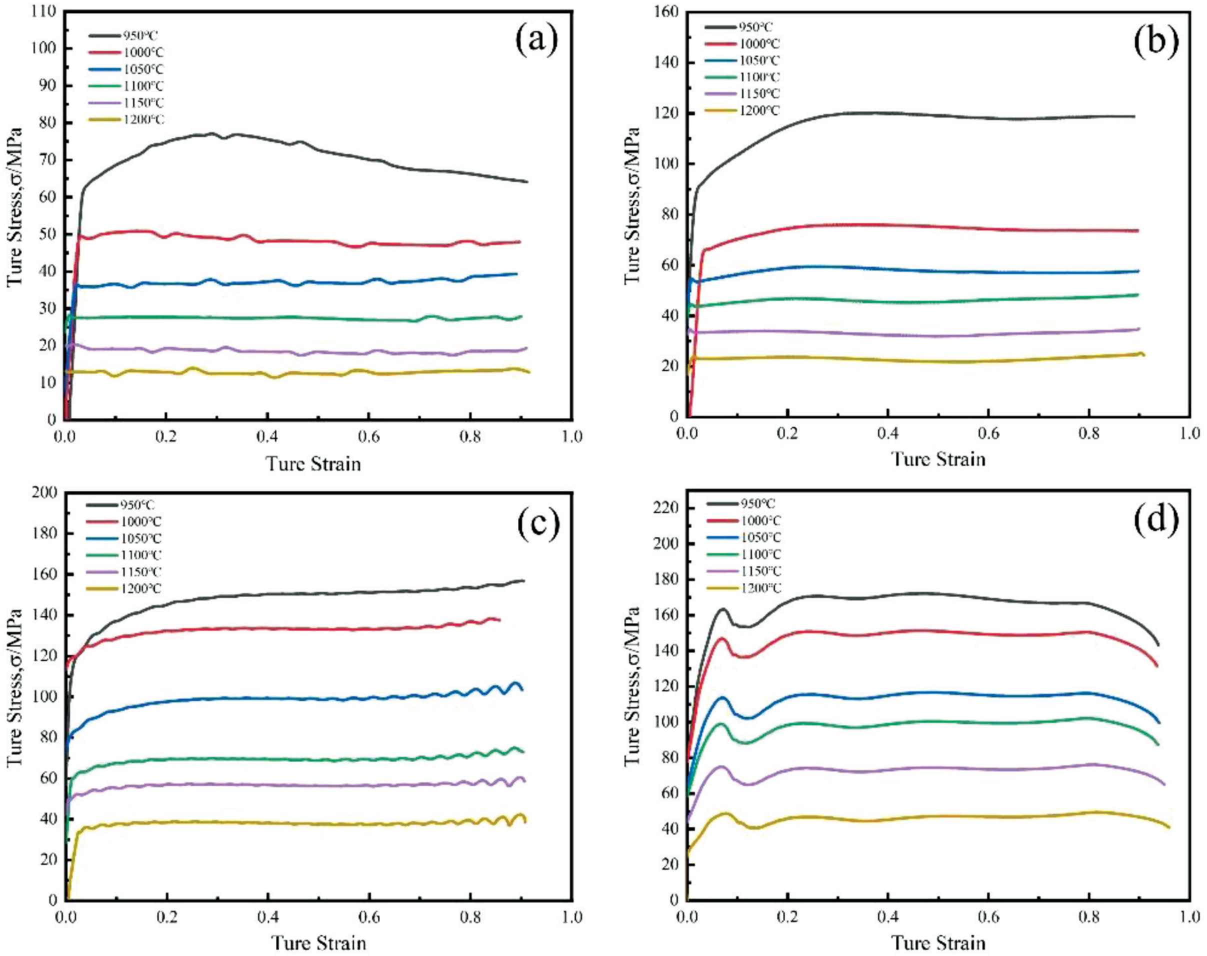

Figure 2: True stress-strain curves of as-cast S32101 economical duplex stainless steel under different conditions: a) 0.01 s^{-1}, b) 0.1 s^{-1}, c) 1 s^{-1}, d) 10 s^{-1}

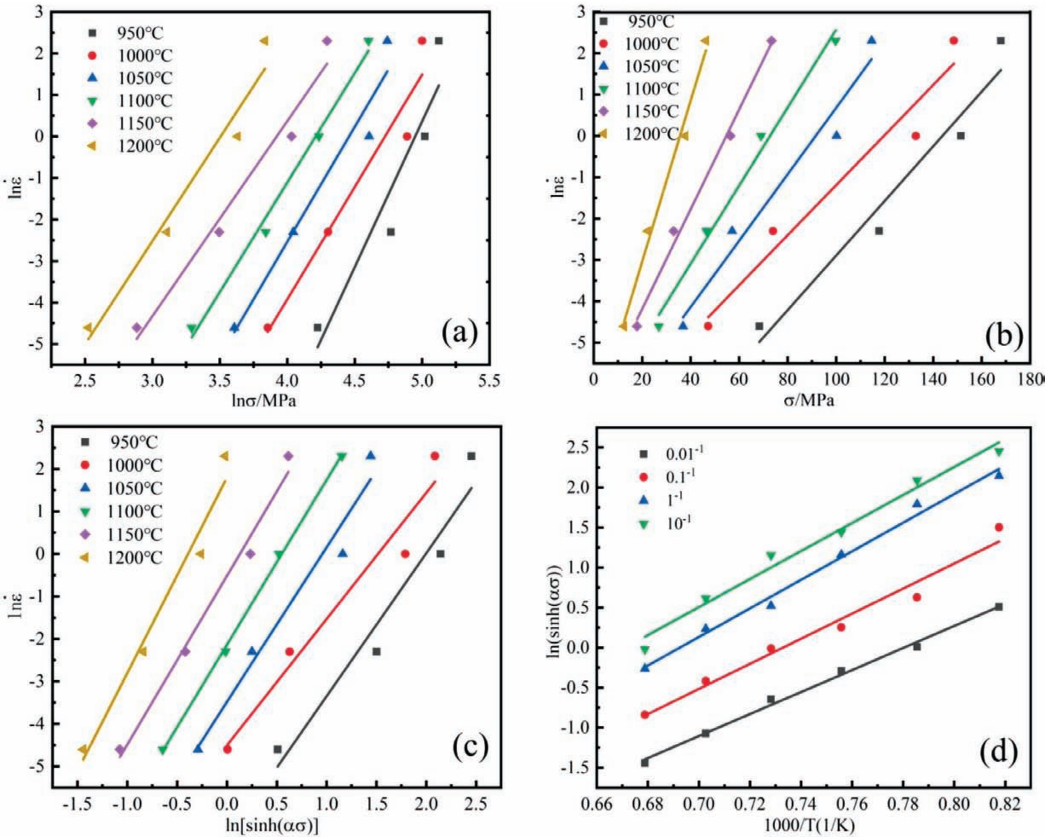

Figure 3: a) Linear fitting $\ln\dot{\varepsilon}-\ln\sigma$, b) linear fitting $\ln\dot{\varepsilon}-\sigma$, c) linear fitting $\ln\dot{\varepsilon}-\ln\left[\sin(\alpha\sigma)\right]$, d) linear fitting $\ln\left[\sin(\alpha\sigma)\right]-1000T^{-1}$

3.2 Establishment of the constitutive equation

The Arrhenius-type constitutive equation is widely used to explain the influence of deformation temperature and strain rate on stress during thermal deformation.[15]

$$\ln\dot{\varepsilon}=\ln A+n\left[\ln\sinh(\alpha\sigma)\right]-\frac{Q}{RT},\quad \text{for all} \tag{1}$$

$$\ln\dot{\varepsilon}=\ln A_1+n_1\ln\sigma-\frac{Q}{RT},\quad \text{for } \alpha\sigma<0.8 \tag{2}$$

$$\ln\dot{\varepsilon}=\ln A_2+\beta s-\frac{Q}{RT},\quad \text{for } \alpha\sigma>1.2 \tag{3}$$

Here, $\dot{\varepsilon}$ is the strain rate; σ is the stress; A_1, A_2, A_3, n_1, n, α, and β are the material constants; $\beta=\alpha n_1$; Q is the activation energy (KJ/mol); T is the absolute temperature (K); and R is the gas constant ($8.31\,\mathrm{J\cdot mol^{-1}\cdot k^{-1}}$).

In general, Equation (1) applies to the entire stress range while Equations (2) and (3) can be used for low and high stress levels, respectively. This constitutive model can be represented by the Zener-Hollomon parameter (Z), namely:

$$Z=\dot{\varepsilon}\exp\left(\frac{Q}{RT}\right)=A\left[\sinh(\alpha\sigma)\right]^n \tag{4}$$

Deform Equation (5) is used:

$$\sigma=\frac{1}{\alpha}\ln\left\{\left(\frac{Z}{A}\right)^{\frac{1}{n}}+\left[\left(\frac{Z}{A}\right)^{\frac{2}{n}}+1\right]^{\frac{1}{2}}\right\} \tag{5}$$

Strain values of 0.05–0.90 were taken at intervals of 0.05, resulting in a total of 18 data groups. In this study, only the strain value of 0.45 is used as an example for the calculation steps.

Firstly, $\ln\dot{\varepsilon}-\ln\sigma$ and $\ln\dot{\varepsilon}-\sigma$ were plotted for linear fitting, as shown in **Figures 3a** and **3b**, whose average slopes are n_1 and β, respectively, and the value of α can be obtained from $\beta=\alpha n_1$. The value of α is substituted into Equation (1), and then linear fitting is performed on $\ln\dot{\varepsilon}-\ln[\sinh(\alpha\sigma)]$, as shown in **Figure 3c**. The average slope is n, and the average intercept is $\ln A-Q/RT$. In general, the solution formula for the value of Q is $Q=1000\,nRk$, and k is the average slope value of the linear fit of $\ln[\sinh(\alpha\sigma)]-1000/T$. Finally, $\ln A$ can be obtained using the value of Q calculated previously.

Equation (5) does not consider the influence of strain on flow stress in the process of high-temperature deformation, and there is no correlation between the solved parameter values; the model's applicability is limited. It is, therefore, necessary to fit the parameters into a function of strain. As shown in **Figure 4**, its fitting equation is expressed as follows:

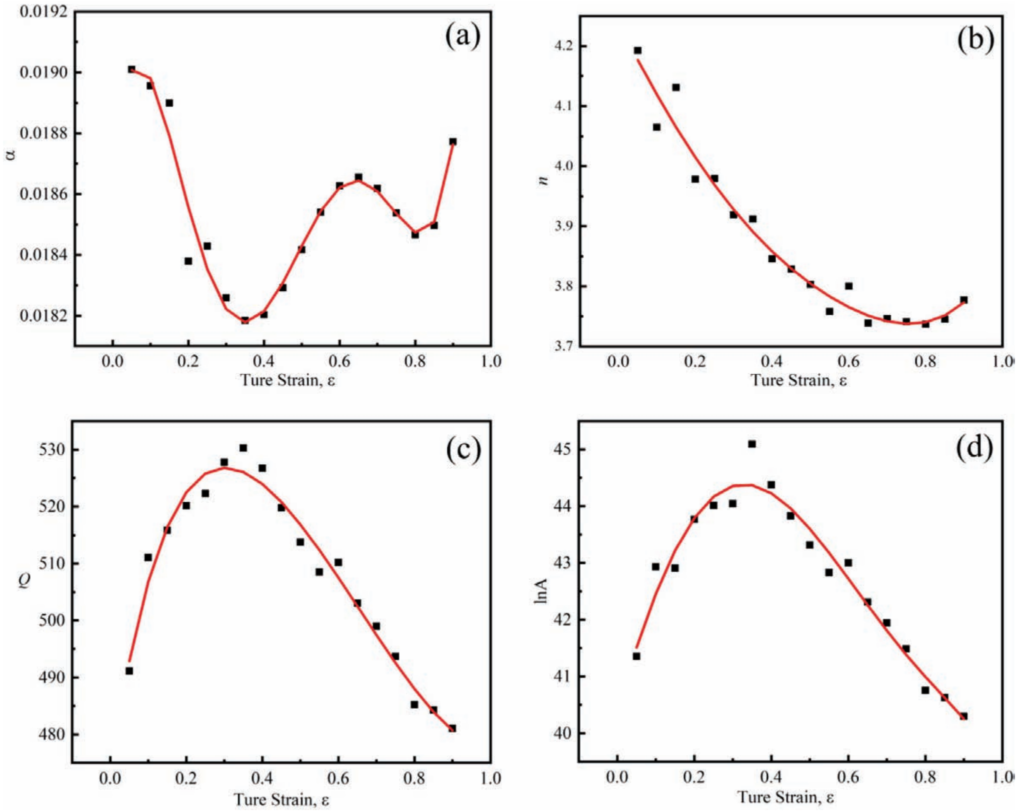

Figure 4: Changes in the material constants with true strain: a) α-ε, b) n-ε, c) Q-ε, d) ln$A$-ε

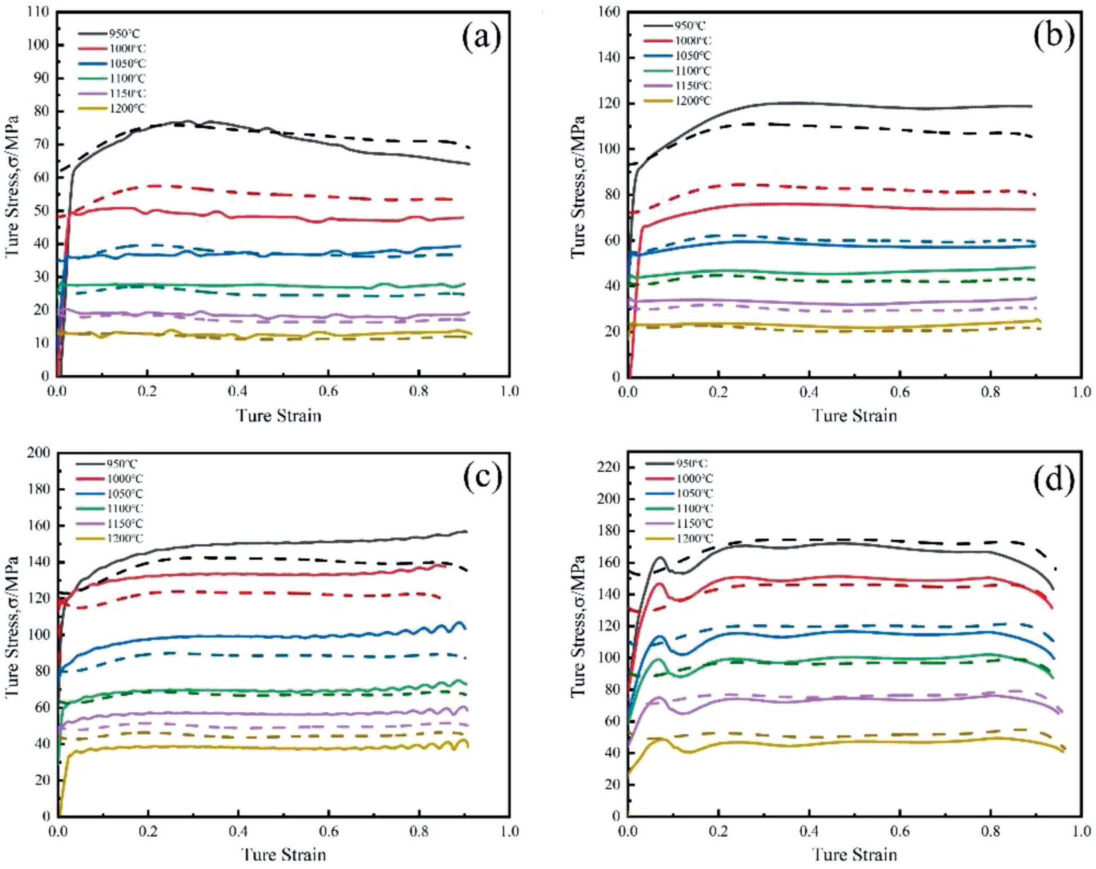

Figure 5: Comparison between experimental values and predicted values: a) 0.01 s^{-1}, b) 0.1 s^{-1}, c) 1 s^{-1}, d) 10 s^{-1}

$$\alpha = \mathrm{B}(\varepsilon) = 0.01642 - 0.08815\varepsilon - 0.94184\varepsilon^2 + 4.50676\varepsilon^3 - 11.4611\varepsilon^4 + 16.09016\varepsilon^5 - 11.76019\varepsilon^6 + 3.4893\varepsilon^7$$

$$n = \mathrm{C}(\varepsilon) = 4.34301 - 4.53738\varepsilon + 34.00634\varepsilon^2 - 155.881\varepsilon^3 + 383.4748\varepsilon^4 - 510.092\varepsilon^5 + 346.9308\varepsilon^6 - 94.4146''\ \varepsilon^7$$

$$Q = \mathrm{D}(\varepsilon) = 443.53895 + 1470.36182\varepsilon - 12877.78513\varepsilon^2 + 62194.3141\varepsilon^3 - 166641.11275\varepsilon^4 + 244251.16512\varepsilon^5 - 183476.13877\varepsilon^6 + 55234.62631\varepsilon^7$$

$$\ln A = E(\varepsilon) = 37.89926 + 109.86208\varepsilon - 1013.81676\varepsilon^2 + 5167.51851\varepsilon^3 - 14313.55706\varepsilon^4 + 21370.23883\varepsilon^5 - 16215.0448\varepsilon^6 + 4907.46639\varepsilon^7 \quad (6)$$

The SCA constitutive model of the as-cast S32101 economical duplex stainless steel is solved at this point. According to Equations (5) and (6), the primary prediction function of its stress is as follows:

$$\sigma = \frac{1}{B(\varepsilon)} \ln\left\{ \left[\frac{\dot{\varepsilon} \exp(D(\varepsilon) / RT)}{\exp[(E(\varepsilon)]} \right]^{\frac{1}{C(\varepsilon)}} + \left(\left[\frac{\dot{\varepsilon} \exp(D(\varepsilon) / RT)}{\exp[(E(\varepsilon)]} \right]^{\frac{2}{C(\varepsilon)}} + 1 \right)^{\frac{1}{2}} \right\} \quad (7)$$

The calculation of the flow stress prediction map is shown in **Figure 5**.

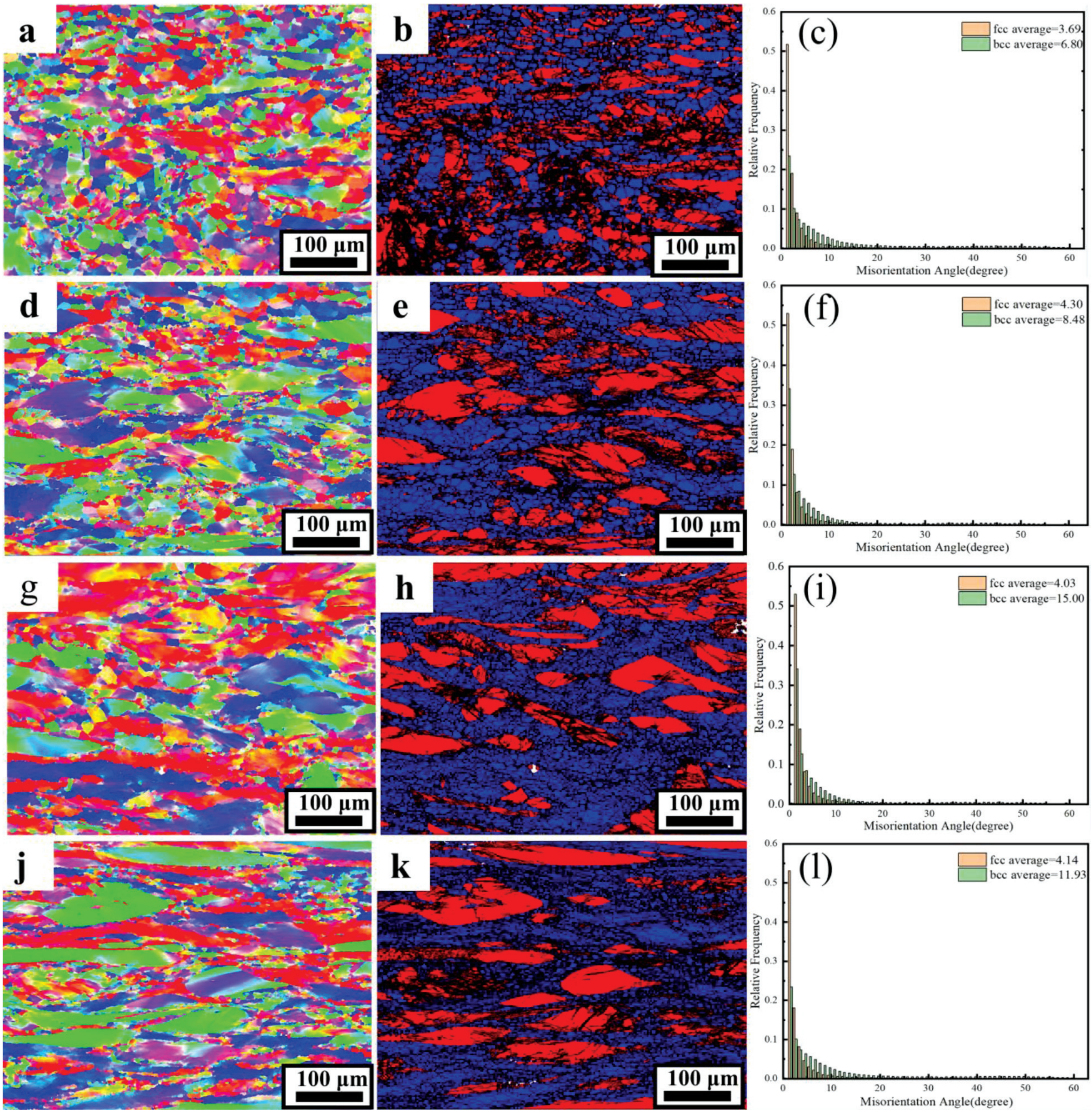

Figure 6: S32101 economical duplex stainless steel at 950 °C: a, b, c) 0.01 s^{-1}; d, e, f) 0.1 s^{-1}; g, h, i) 1 s^{-1}; j, k, l) 10 s^{-1} EBSD IPFs, EBSD phase map BCC (blue) and FCC (red)+ grain boundary, grain boundary orientation deviation distribution map; (the black thin solid line is the low-angle grain boundary (2–15°), the black thick solid line is the high-angle grain boundary (>15°))

3.3 Microstructure evolution

Figure 6 shows an EBSD inverse pole figure (IPF), EBSD phase maps for BCC (blue) and FCC (red), and the misorientation distribution of grain boundaries for S32101 economical duplex stainless steel at a deformation temperature of 950 °C under different strain rates. In the phase maps, fine black lines represent low-angle grain boundaries (LAGBs) with misorientation angles between 2° and 15°, while thick black lines indicate high-angle grain boundaries (HAGBs) with misorientations greater than 15°. As seen in **Figure 6b**, under a strain rate of 0.01 s^{-1}, there are more recrystallized grains, and the grain size is relatively uniform. This is because, at lower strain rates, the energy provided by strain is mostly consumed by the BCC phase, with little or no energy being transferred to the FCC phase. As the strain rate increases to 0.1–10 s^{-1}, at higher strain rates, elongation occurs in the vertical compression direction. Due to the low temperature and high strain rate, almost no recrystallization occurs, and LAGBs increase. The grain boundary misorientation distribution is plotted

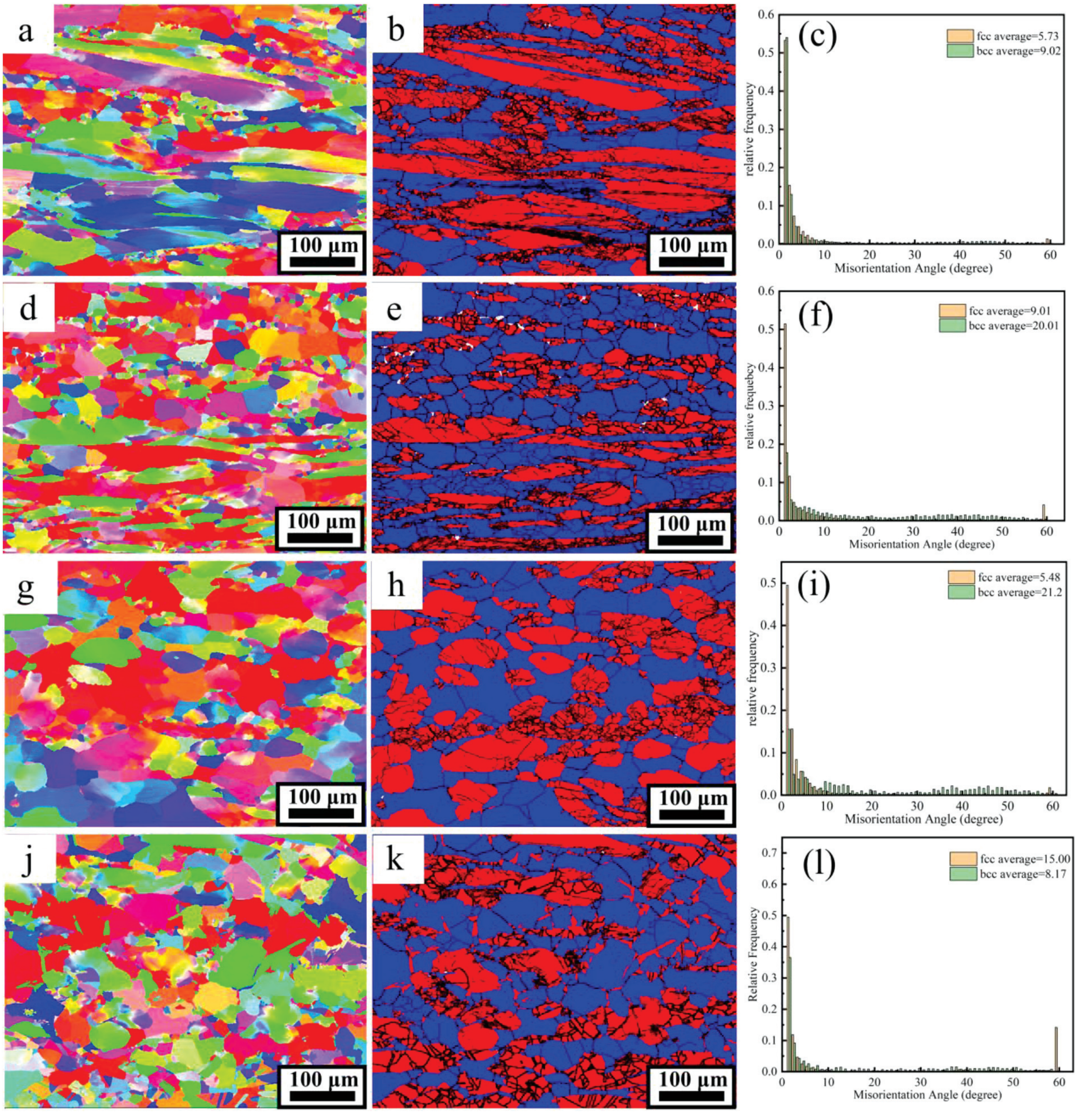

Figure 7: S32101 economical duplex stainless steel at 1100 °C: a, b, c) 0.01 s^{-1}; d, e, f) 10 s^{-1}, 1150 °C; g, h, i) 0.01 s^{-1}; j, k, l) 10 s^{-1} EBSD IPFs, EBSD phase map BCC (blue) and FCC (red)+ grain boundary, grain boundary orientation deviation distribution map, (black thin solid line is the low-angle grain boundary (2–15°), black thick solid line is the high-angle grain boundary (>15°))

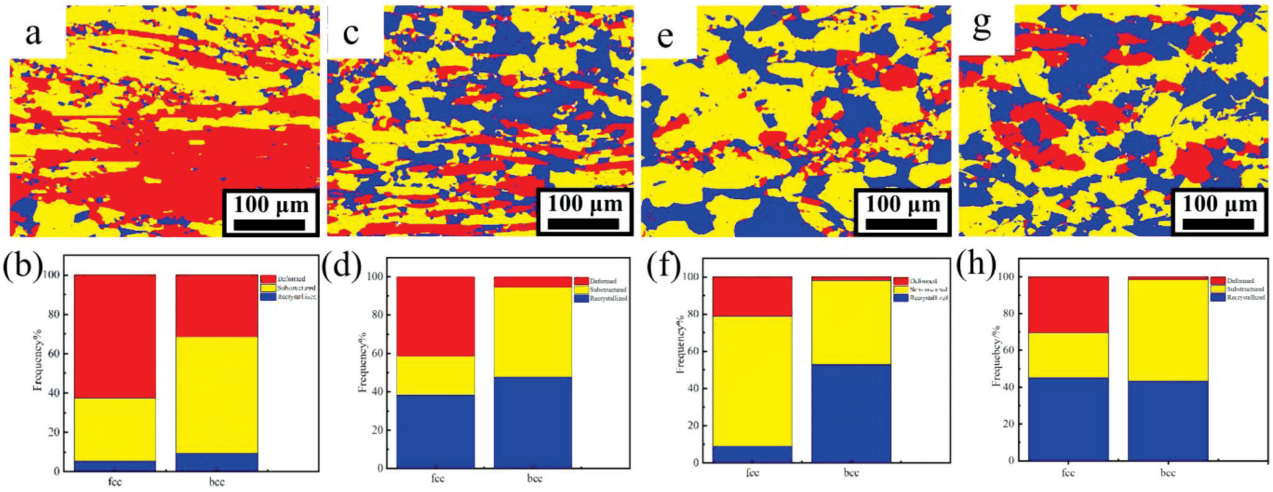

Figure 8: Recrystallization map: a, b) 1100 °C /0.01 s^{-1}; c, d) 1100 °C /10 s^{-1}; e, f) 1150 °C /0.01 s^{-1}; g, h) 1150 °C /10 s^{-1}

based on the EBSD analysis. At the lower temperature (950 °C), the misorientation distribution of grain boundaries under different strain rates is concentrated at large-angle boundaries (2–15°), and the average misorientation between FCC and BCC does not exceed 15°. This indicates that most of the structure consists of subgrain boundaries. Additionally, strain hardening can be observed in the stress-strain curves at 950 °C.

As the temperature increases, the proportion of LAGBs (low-angle grain boundaries) gradually decreases, especially under high strain rates. As shown in **Figures 7a** and **7b**, the as-cast microstructure at 1100 °C/0.01 s^{-1} exhibits severe deformation, with numerous LAGBs still present within the grains. When the strain rate increases to 10 s^{-1}, the DRX (dynamic recrystallization) fractions of both phases rise sharply, the recrystallized grains grow, and the BCC microstructure becomes more homogeneous. This microstructural evolution is primarily attributed to the substantial driving force generated under high temperatures and high strain rates, which accelerates the conversion of LAGBs into HAGBs (high-angle grain boundaries), thereby promoting DRX.[16]

Notably, at 1150 °C, the FCC recrystallized grains grow and exhibit an equiaxed structure at a strain rate of 0.01 s^{-1}. However, when the strain rate increases to 10 s^{-1}, the FCC phase shows an increased fraction of twin boundaries, as evident in the misorientation distribution maps for 2–15° (**Figure 7l**). The peak shifts upward with increasing strain rate, indicating an increase in the twin formation.[17] At 1150 °C/10 s^{-1}, the presence of twins is evident, as shown in **Figure 7k**. According to reference,[18] twins can facilitate the formation of dynamic recrystallization, reduce energy consumption, refine grains, and improve the alloy's ductility. Comparing **Figures 7d** and 8j, it can be observed that at 10 s^{-1}, the FCC phase at 1100 °C exhibits partial elongation, attributed to the uneven stress distribution during rapid deformation. Under deformation conditions at 1150 °C, the two phases show no significant elongation. The results indicate that high temperatures lead to more coordinated deformation between the two phases. Under identical deformation conditions, ferrite, with a relatively high SFE (stacking fault energy), facilitates dislocation climb and slip, reducing deformation resistance and promoting substructure formation during thermal deformation. When the BCC phase undergoes thermal deformation, dislocations are prone to cross-slip or climb, leading to rearrangement or annihilation of some dislocations, thereby reducing the BCC dislocation density.

Figure 8 shows the recrystallization maps of S32101 duplex stainless steel at 1100 °C and 1150 °C, and strain rates of 0.01 s^{-1} and 10 s^{-1}. In the maps, blue represents recrystallization, yellow represents substructures, and red represents deformation. At low strain rates, red deformation and yellow substructures dominate, while blue recrystallization occupies a relatively small fraction. This is because at low strain rates, the deformation energy is relatively low, hindering the formation of dynamic recrystallization (DRX). At the same time, blue recrystallization mainly occurs in the BCC phase, indicating that under the same deformation conditions, BCC is more likely to undergo recrystallization than FCC. This is because austenite, with a low stacking fault energy (SFE), cannot soften directly through recovery without a nucleation period due to the dislocation tangling and vacancy defects generated during hot deformation, and there is a certain delay in the recrystallization process. During hot deformation, ferrite generally accommodates the strain first, and only after it reaches a certain deformation level is the strain gradually transferred to the austenite phase. The accumulated deformation needs to reach a sufficient energy threshold for the recrystallization to occur. When the strain rate increases to 10 s^{-1}, the recrystallization of both phases increases. At 1100 °C, the recrystallization fractions of FCC and BCC are 38.44 % and 47.81 %, respectively, while at 1150 °C, the recrystallization fractions are 45.04 % and 43.34 %,

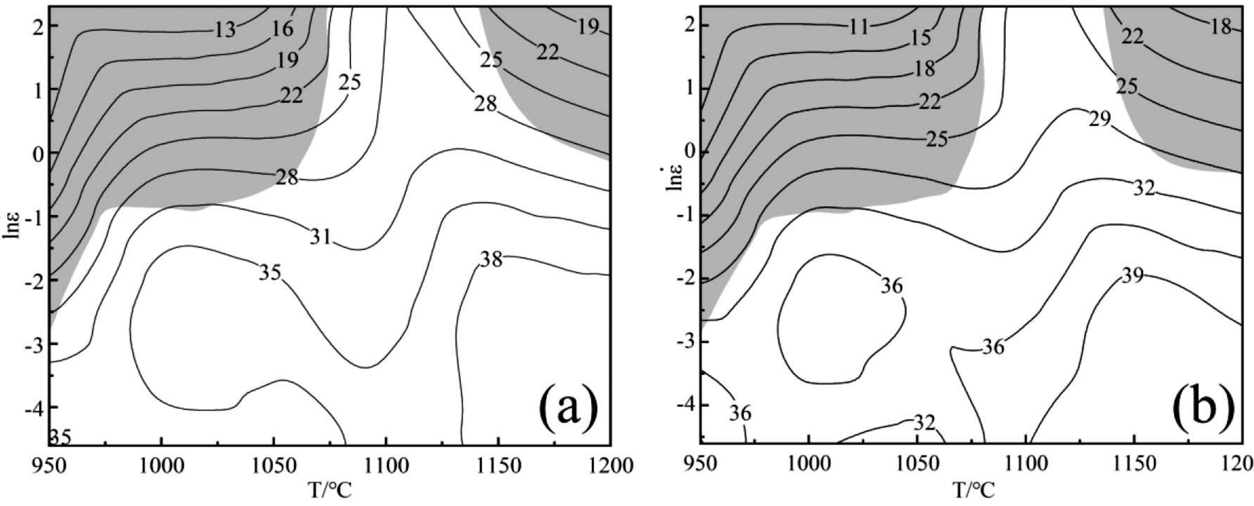

Figure 9: Processing maps at different true strains: a) 0.3, b) 0.7

respectively. Song et al.[12] plotted the recrystallization fractions of both phases of 2205 duplex stainless steel under different deformation conditions. In the deformation of 2205 duplex stainless steel, high strain rates improved atomic diffusion and migration abilities, thereby promoting recrystallization, which is consistent with the dual-phase recrystallization observed in this study.

3.4 Processing maps

The dynamic material model (DMM) hot-working diagram is constructed based on the power dissipation and material instability under various thermal deformation parameters, offering a visual representation of the material's processing behavior. According to the DMM theory, the total energy (*P*) supplied by external sources during material deformation can be divided into two components: the energy used for plastic deformation (*G*) and the energy utilized for the evolution of the material's microstructure (J).

$$P = \sigma\dot{\varepsilon} = G + J = \int_0^{\dot{\varepsilon}} \sigma \mathrm{d}\dot{\varepsilon} + \int_0^{\sigma} \dot{\varepsilon} \mathrm{d}\sigma \tag{8}$$

Under the given processing conditions, the relationship between the stress and strain rate of the material can be expressed by a set of dynamic equations as follows:

$$\sigma = K\dot{\varepsilon}^{\mathrm{m}} \tag{9}$$

Here, *K* expresses the material constant, $\dot{\varepsilon}$ represents the strain rate, σ denotes the flow stress, m represents the strain rate sensitivity, whose calculation equation is:

$$m = \frac{\partial J}{\partial G} = \frac{\dot{\varepsilon}\partial\sigma}{\sigma\partial\dot{\varepsilon}} = \frac{\partial \ln\sigma}{\partial \ln\dot{\varepsilon}} \tag{10}$$

If the material is in an ideal linear dissipative state, it corresponds to the maximum value of *J*.

$$J_{\max} = \frac{m}{m+1}\sigma\dot{\varepsilon} = \frac{\sigma\dot{\varepsilon}}{2} = \frac{P}{2} \tag{11}$$

In the DMM, the ratio of energy dissipation to the maximum linear dissipative energy is taken as the material's power dissipation factor, denoted as η. Using the calculated values of η, a power dissipation diagram for the S32101 economical duplex stainless steel under different strains can be plotted:

$$\eta = \frac{J}{J_{\max}} = \frac{2m}{2m+1} \tag{12}$$

Prasad et al.19, using Ziegler's maximum entropy yield principle, proposed an inequality relating dissipative power (D) and strain rate:

$$\frac{\mathrm{d}D}{\mathrm{d}\dot{\varepsilon}} < \frac{D}{E} \tag{13}$$

According to the DMM theory, the instability criterion during the material's thermal deformation can be transformed into

$$\xi(\dot{\varepsilon}) = \frac{\partial \ln(m/m+1)}{\partial \ln\dot{\varepsilon}} + m < 0 \tag{14}$$

When the instability parameter ξ has a negative value, it corresponds to the unstable region as proposed by Prasad's theory. Combining the power dissipation diagram and the instability diagram obtained during the calculation, the thermal-working diagram for S32101 economical duplex stainless steel can be overlaid and plotted, as shown in **Figure 9**.

Figure 9 illustrates the processing maps at true strains of 0.3 and 0.7. The regions with the instability factor (ξ) < 0, indicated as gray areas, are referred to as unstable processing zones. These regions are associated with potential risks of non-uniform deformation, such as cracking, and should be avoided. Conversely, regions with (ξ) > 0, indicated as white areas, are identified as thermally stable zones. At true strains of 0.3 and 0.7, unstable processing zones are primarily observed at 950–980 °C/0.02–10 s^{-1}, 980–1075 °C/0.2–10 s^{-1}, and 1125–1200 °C/0.4–10 s^{-1}. In the stable zones, the peak dissipation factor is approximately 0.39, occurring within a temperature range of 1145–1200 °C and strain rates of 0.01–0.1 s^{-1}. Therefore, the optimal hot-deformation domains are identified as 1000–1200 °C/0.01–0.2 s^{-1} and 1095–1130 °C/0.01–10 s^{-1}.

4 CONCLUSIONS

The hot-deformation behavior of as-cast S32101 economical duplex stainless steel was investigated within a temperature range of 950–1200 °C and strain rates of 0.1–10 s^{-1}. The key findings are summarized as follows:

1. At 950 °C, a clear yield plateau is observed on the flow curve under strain rates of 0.01 s^{-1} and 0.1 s^{-1}. This plateau behavior, commonly observed in low-carbon and low-strength low-alloy steels, is primarily attributed to the 'dragging' effect of C-N atomic clusters (Cottrell atmospheres) on dislocations.

2. The high-precision strain-compensated Arrhenius constitutive model of S32101 economical duplex stainless steel is established:

$$\sigma = \frac{1}{B(\varepsilon)} \ln \left\{ \left[\frac{\dot{\varepsilon} \exp(D(\varepsilon) / RT)}{\exp[(E(\varepsilon)]} \right]^{\frac{1}{C(\varepsilon)}} + \left(\left[\frac{\dot{\varepsilon} \exp(D(\varepsilon) / RT)}{\exp[(E(\varepsilon)]} \right]^{\frac{2}{C(\varepsilon)}} + 1 \right)^{\frac{1}{2}} \right\} \tag{7}$$

$\alpha = B(\varepsilon) = 0.01642 - 0.08815\varepsilon - 0.94184\varepsilon^2 + 4.50676\varepsilon^3 - 11.4611\varepsilon^4 + 16.09016\varepsilon^5 - 11.76019\varepsilon^6 + 3.4893\varepsilon^7$

$n = C(\varepsilon) = 4.34301 - 4.53738\varepsilon + 34.00634'' \varepsilon^2 - 155.881\varepsilon^3 + 383.4748\varepsilon^4 - 510.092 \varepsilon^5 + 346.9308 \varepsilon^6 - 94.4146'' \varepsilon^7$

$Q = D(\varepsilon) = 443.53895 + 1470.36182\varepsilon - 12877.78513\varepsilon^2 + 62194.3141\varepsilon^3 - 166641.11275\varepsilon^4 + 244251.16512\varepsilon^5 - 183476.13877\varepsilon^6 + 55234.62631\varepsilon^7$

$\ln A = E(\varepsilon) = 37.89926 + 109.86208\varepsilon - 1013.81676\varepsilon^2 + 5167.51851\varepsilon^3 - 14313.55706\varepsilon^4 + 21370.23883\varepsilon^5$ $16215.0448\varepsilon^6 + 4907.46639\varepsilon^7$

3. At 1100 °C and 1150 °C/10 s^{-1}, the recrystallization fractions of both phases increase significantly, with the austenite recrystallization showing a positive correlation with strain rate. At the low temperature of 950 °C, the effect of strain rate on recrystallization is minimal due to the slow migration of grain boundaries. Austenite undergoes typical discontinuous dynamic recrystallization (DDRX), while the ferrite phase softens through continuous dynamic recrystallization (CDRX).

4. Based on the hot processing map, the optimal processing windows for S32101 economical duplex stainless steel are determined to be 950–1200 °C/0.01 s^{-1} and 1100 °C/0.01–10 s^{-1}.

CRediT authorship contribution statement

Ming Zhao: Investigation, Methodology, Writing – original draft. Huaying Li: Supervision, Resources, Writing – review & editing. Guanzheng Su: Data curation, Writing – review & editing. Fang Huang Investigation, Visualization. Yibo Lu Investigation, Validation, Writing – review & editing. Qi Chen: Investigation, Validation.

Declaration of Competing Interest

The authors declare that they have no known competing financial interests or personal relationships that could appear to influence the work reported in this paper.

Data availability

Data will be made available on request.

Acknowledgements

This project has been supported by Shanxi Provincial Key Research and Development Project (202202050201015), Shanxi Provincial Scientific Research Practice Innovation Project (2023SJ241), Shanxi Provincial Scientific and Technological Achievements Guiding Special Project (202204021301057), Central Guiding Local Science and Technology Development Fund Project (YDZJSX2021A036), as well as Graduate Education Innovation Project of Taiyuan University of Science and Technology (SY2023036).

5 REFERENCES:

[1] L. Ma, S. S. Hu, J. Q. Shen, Microstructure, Properties and Weldability of Duplex Stainless Steel 2101, J. Mater. Eng. Perform., 26 (**2017**), 250–257, doi:10.1007/s11665-016-2428-2

[2] S. Patra, A. Agrawal, A. Mandal, A. S. Podder, Characteristics and Manufacturability of Duplex Stainless Steel: A Review, Trans. Indian Inst. Met., 74 (**2021**) 5, 1089–1098, doi:10.1007/s12666-021-02278-7

[3] C. G. Bao, C. Zhang, Preparation and corrosion resistance properties of duplex stainless steel (00Cr22Ni6MnMoCu), Mater. Res. Express, 8 (**2021**) 12, 126501, doi:10.1088/2053-1591/ac3bf8

[4] X. C. Ma, Z. J. An, L. Chen, T. Q. Mao, J. F. Wang, H. J. Long, H. Y. Xue, The effect of rare earth alloying on the hot workability of duplex stainless steel – A study using processing map, Mater. Des., 86 (**2017**), 848–854, doi:10.1016/j.matdes

[5] B. O. Okonkwo, H. L. Ming, Z. M. Zhang, J. Q. Wang, E. Rahimi, S. Hosseinpour, A. Davoodi, Microscale investigation of the correlation between microstructure and galvanic corrosion of low alloy steel A508 and its welded 309/308L stainless steel overlayer, Corros. Sci., 154 (**2019**), 49–60, doi:10.1016/j. corsci

[6] Q. Xiong, H. J. Li, Z. P. Lu, J. J. Chen, Q. Xiao, J. R. Ma, X. K. Ru, Characterization of microstructure of A508III/309L/308L weld and oxide films formed in deaerated high-temperature water, J. Nucl. Mater., 498 (**2018**), 227–240, doi:10.1016/j.jnucmat

[7] A. Abbasi-Bani, A. Zarei-Hanzaki, M. H. Pishbin, N. Haghdadi, A comparative study on the capability of Johnson–Cook and Arrhenius-type constitutive equations to describe the flow behavior of Mg–6Al–1Zn alloy, Mech. Mat., 71 (**2014**), 52–61, doi:10.1016/j.mechmat

[8] Z. Sangari Motlagh, B. Tolaminejad, A. Momeni, Prediction of Hot Deformation Flow Curves of 1.4542 Stainless Steel, Met. Mater. Int., 27 (**2021**) 2512–2529, doi:10.1007/s12540-020-00627-7

[9] Y. C. Lin, X. M. Chen, G. Liu, A modified Johnson–Cook model for tensile behaviors of typical high-strength alloy steel, Mater. Sci. Eng. A, 527 (**2010**), 6980–6986, doi:10.1016/j.msea.2010.07.061

[10] D. Samantaray, S. Mandal, A. K. Bhaduri, A thermo-viscoplastic constitutive model to predict elevated-temperature flow behaviour in a titanium-modified austenitic stainless steel, Mater. Sci. Eng. A, 47 (**2009**), 568–576, doi:10.1016/j.commatsci

[11] X. Lin, H. Huang, X. Yuan, Y. Wang, B. Zheng, X. Zuo, Establishment and validity verification of the hot processing map of a Ti-47.5Al-2.5V-1.0Cr-0.2Zr alloy with a lamellar microstructure, Mater. Charact., 183 (**2022**), 111599, doi:10.1016/j.matchar.2021.111599

[12] Y. H. Song, Y. G. Li, G. H. Zhao, H. T. Liu, H. Y. Li, J. Li, E. Q. Liu, Electron Backscatter Diffraction Investigation of Heat Deformation Behavior of 2205 Duplex Stainless Steel, Steel Res. Int., 92 (**2021**) 5, https://onlinelibrary.wiley.com/doi/full/10.1002/srin.202000587

[13] Y. Cai, S. Xiang, Y. Tan, Insight into the Dynamic Recrystallization Behavior and Microstructure Evolution of MP159 Superalloy During Hot Deformation, Met. Mater. Int., 28 (**2022**), 2381–2394, doi:10.1007/s12540-021-01139-8

[14] L. Chen, X. C. Ma, X. Liu, L. M. Wang, Processing map for hot working characteristics of a wrought 2205 duplex stainless steel, Mater. & Des., 32 (**2011**) 3, doi:10.1016/j.matdes.2010.09.030

[15] J. J. Jonas, C. M. Sellars, W. J. M. G. Tegart, Strength and structure under hot-working conditions. Metall. Rev., 14 (**1969**) 1

[16] Y. Lu, H. B. Xie, J. Wang, Z. Li, F. H. Jia, H. Wu, J. T. Han, Z. Y. Jiang, Influence of hot compressive parameters on flow behaviour and microstructure evolution in a commercial medium carbon micro-alloyed spring steel, J. Manuf. Process., 58 (**2020**), 1171–1181, doi:10.1016/j.jmapro.2020.09.021

[17] Y. H. Song, Z. H. Cai, G. H. Zhao, Y. G. Li, H. Y. Li, M. X. Zhang, Hot deformation behavior of 309L stainless steel, Mater. Today Commun., 36 (**2023**), 106877, doi:10.1016/j.mtcomm.2023.106877

[18] J. Li, G. H. Zhao, L. F. Ma, H. Q. Chen, H. Y. Li, Q. X. Huang, W. Zhang, Hot deformation behavior and microstructural evolution of as-cast 304L antibacterial austenitic stainless steel, Mater. Res. Express, 5 (**2017**) 2, 2–9, https://iopscience.iop.org/article/10.1088/2053-1591/aaa445

[19] N. Srinivasa, Y. V. R. K. Prasad, Hot working characteristics of nimonic 75, 80A and 90 superalloys: a comparison using processing maps, J. Mater. Process. Technol., 51 (**1995**), 171–192, doi:10.1016/0924-0136(94)01602-W